Applied Thermal Engineering 183 (2021) 116205

Contents lists available at ScienceDirect

Applied Thermal Engineering

journal homepage: www.elsevier.com/locate/apthermeng

# A study on flow and heat transfer characteristics of a constructal bifurcation filler in the circular tube

Minjie Yu, Xiaotian Lai, Hui Xiao, Zhichun Liu, Wei Liu *

*School of Energy and Power Engineering, Huazhong University of Science and Technology, Wuhan 430074, China*

ARTICLE INFO

*Keywords:*
Constructal bifurcation
Porous media
Filler
Flow resistance
Heat transfer

ABSTRACT

Porous media are applied extensively in energy systems. However, the large flow resistance caused by porous media restricts the energy utilization and conversion efficiency. To reduce flow resistance, a constructal bifurcation filler was proposed as an alternative to the porous media filler based on constructal concept and fluid disturbance intensification idea. The two fillers were fitted in the circular tubes to investigate and compare their thermo-hydraulic characteristics. The fluid flow and heat transfer mechanisms of the two types of tubes were analyzed. The fluid disturbance intensification is the dominant mechanism of the heat transfer enhancement in the tube with the constructal bifurcation filler. Moreover, the flow resistance of the tube with the constructal bifurcation filler is decreased significantly, by 78.51–93.33%, compared to the tube with the porous media filler. Meanwhile, in contrast to the traditional fluid disturbance intensification elements, an excellent temperature uniformity similar to that of porous media is obtained for the constructal bifurcation filler. Furthermore, the efficiency evaluation criteria value is 3.66–8.77. Thus, the constructal bifurcation filler was demonstrated to exhibit superior comprehensive performance and is an effective solution for diminishing the flow resistance and improving the energy utilization efficiency. Finally, the effects of structure parameters, such as the wire mesh pitch $s$ and inclined angle $\alpha$, on the thermo-hydraulic performance of the tube with the constructal bifurcation filler were investigated.

## 1. Introduction

With the increasing demand for energy in recent decades, numerous techniques have been developed to increase the heat transfer rate, improve the energy utilization efficiency, and reduce the system size [1]. These techniques have included the employment of fins [2,3], rough surfaces [4], different inserts [5–9], micro/nanostructures [10,11], porous media, and desiccant coating [12]. Among these, porous media have attracted substantial attention owing to their light weight, low cost, large heat transfer area, high effective thermal conductivity, and excellent temperature uniformity [1,13]. As a result of the above-mentioned advantages, porous media have been applied extensively in energy fields such as waste heat recovery, electronic cooling, porous media combustion, solar heat collection, and heat accumulation [14].

Various investigations on applying porous media as fillers to increase the heat transfer rate of heat exchangers have demonstrated that such materials play a significant role in heat transfer enhancement. Dehghan et al. [15] enhanced the heat transfer of micro-channels by inserting porous material. The comprehensive performance was found to be effectively increased by inserting porous media with a high porosity. Mohammadi et al. [16] conducted a numerical investigation to analyze the effects of the permeability, porosity, and baffle cut of porous baffles on the heat transfer rate and pressure drop of a shell and tube heat exchanger. The results demonstrated that a porous baffle with higher heat transfer generated larger pressure drop. Huang et al. [17] enhanced the heat transfer in the core flow by inserting porous media in the duct. The flow resistance and heat transfer performance of the airflow from a laminar to a fully turbulent regime were experimentally and numerically investigated for various porosities. The results revealed that porous media inserts improved the heat transfer performance, however, greater flow resistance was induced. Sheikholeslami et al. [18] accelerated the solidification in a new thermal heat storage system by inserting porous media. The heat transfer between the air and the phase change material was enhanced by the insertion of the porous media. The energy storage unit with porous media achieved a 21.4% faster solidification duration compared to that without porous media.

The heat transfer and pressure drop characteristics of supercritical $CO_2$ through metal foam in a tube were experimentally investigated by Liu et al. [19]. The effects of the $CO_2$ mean bulk temperature, mass flow

* Corresponding author.
*E-mail address:* w_liu@hust.edu.cn (W. Liu).

https://doi.org/10.1016/j.applthermaleng.2020.116205
Received 9 June 2020; Received in revised form 7 October 2020; Accepted 9 October 2020
Available online 14 October 2020

**Nomenclature**

| | |
|---|---|
| $A_i$ | inlet flow area, $m^2$ |
| $C_{1\varepsilon}$,$C_{2\varepsilon}$ | turbulent model coefficients |
| $C_2$ | inertial resistance coefficient, $m^{-1}$ |
| $c_f$ | friction factor based on hydraulic diameter |
| $c_p$ | specific heat at constant pressure, J/(kg·K) |
| $D$ | tube diameter, mm |
| $d_1$ | filler diameter, mm |
| $d_2$ | central circular rod diameter, mm |
| $d_3$ | wire diameter, mm |
| $d_h$ | hydraulic diameter, m |
| $EEC$ | efficiency evaluation criterion |
| $f$ | friction factor of the T-CBF based on tube diameter |
| $f_p$ | friction factor of the T-PMF based on tube diameter |
| $G_k$ | generation of $k$ due to mean velocity gradient |
| $h$ | heat transfer coefficient, W/($m^2$·K) |
| $h_l$ | heat transfer coefficient per unit length, W/($m^3$·K) |
| $K$ | permeability, $m^2$ |
| $k$ | turbulent kinetic energy, $m/s^2$ |
| $L$ | tube length, mm |
| $Nu$ | Nusselt number of the T-CBF |
| $Nu_p$ | Nusselt number of the T-PMF |
| $Pr$ | Prandtl number |
| $p$ | pressure, Pa |
| $q$ | wall heat flux, $W/m^2$ |
| $r$ | radial position of specific point, mm |
| $R$ | tube radius, mm |
| $Re$ | inlet Reynolds number |
| $Re_h$ | Reynolds number based on hydraulic diameter |
| $S$ | convective heat transfer from solid to fluid, $W/m^3$ |
| $S_f$ | resistance source term, Pa/m |
| $s$ | wire mesh pitch, mm |
| $T$ | local temperature, K |
| $T_f$ | fluid temperature, K |
| $T_{in}$ | mean temperature of fluid at inlet, K |
| $T_m$ | mean temperature of middle cross-section, K |
| $T_{out}$ | mean temperature of fluid at outlet, K |
| $Ts$ | solid temperature, K |
| $T_w$ | wall temperature, K |
| $\boldsymbol{U}$ | fluid velocity vector, m/s |
| $u$ | local velocity, m/s |
| $u_f$ | fluid volume average velocity, m/s |
| $u_{in}$ | mean velocity of fluid at inlet, m/s |
| $u_m$ | mean velocity of middle cross-section, m/s |
| $\overline{u}$ | dimensionless velocity |
| $Y_M$ | contribution of fluctuating dilatation to overall dissipation rate |
| $z$ | $z$ coordinate, mm |
| $\Delta p$ | pressure drop between inlet and outlet, Pa |
| $\Delta T_m$ | logarithmic mean temperature difference between fluid and wall, K |

*Greek symbols*

| | |
|---|---|
| $\alpha$ | inclined angle, ° |
| $\alpha_k$ | inverse effective Prandtl number for $k$ |
| $\alpha_\varepsilon$ | inverse effective Prandtl number for $\varepsilon$ |
| $\rho_f$ | fluid density, $kg/m^3$ |
| $\rho_{in}$ | mean density of fluid at inlet, $kg/m^3$ |
| $\mu_{eff}$ | effective dynamic viscosity, Pa·s |
| $\mu_f$ | fluid dynamic viscosity, Pa·s |
| $\mu_{in}$ | mean dynamic viscosity of fluid at inlet, Pa·s |
| $\lambda_{eff}$ | effective thermal conductivity, W/(m·k) |
| $\lambda_f$ | fluid thermal conductivity, W/(m·k) |
| $\lambda_s$ | solid thermal conductivity, W/(m·k) |
| $\theta$ | dimensionless temperature difference |
| $\varphi$ | porosity |
| $\varepsilon$ | turbulent dissipation rate, $m^2/s^3$ |

rate, inlet pressure, porosity, and pore density on the thermo-hydraulic characteristics were analyzed, and correlations for the heat transfer and friction factor based on experimental data were presented. Tu et al. [20] found that mesh cylinder inserts could achieve a higher heat transfer rate at the same pumping power compared to other inserts. Baragh et al. [21] experimentally investigated the effects of different porous media arrangements on the thermal performance and pressure drop of single-phase flow in a circular channel. Optimal heat transfer enhancement was obtained in a fully filled channel with porous media in both laminar and turbulent flows, whereas a channel filled with an annulus shaped porous media exhibited the best overall performance in turbulent flow. Subsequently, an experimental investigation was conducted on air mist flow in the same channel fitted with porous media [22]. The results demonstrated that mist cooling in porous media could further enhance the heat transfer compared to that of single-phase flow. Cao et al. [23] suspended consecutive conical-mesh inserts in a tube to modulate the flow and temperature fields.

In addition to the heat transfer enhancement of heat exchangers, researchers have focused on other promising applications of porous media, such as porous media burners [24], battery electrodes [25], and regenerators [26]. In those applications, the use of porous media leads to an increased heat transfer area, higher effective thermal conductivity, and greater heat capacity. However, it is worth noting that although porous media offer significant potential for heat transfer and heat accumulation, numerous investigations have indicated that large flow resistance occurs with fluids flowing through the porous media, which will result in a high pressure drop penalty, higher pump power consumption, and consequently, diminished system efficiency. These factors have limited the development and applications of porous materials to a certain degree. Therefore, it is important to design novel fillers with lower flow resistance and moderate heat transfer performance as alternatives to porous media.

A suitable alternative to porous media should exhibit several characteristics, such as: (1) high heat transfer performance or excellent temperature uniformity, (2) smaller flow resistance, (3) uniform spatial distribution, and (4) adjustable porosity. An effective heat transfer enhancement method is required for the first characteristic. Deshmukh et al. [27,28] experimentally investigated the heat transfer and flow characteristics of a circular tube with curved delta wing vortex generator inserts under laminar and turbulent flows, respectively. The fluid in the tube was subjected to intensive disturbance by the vortex generator inserts, which led to a heat transfer enhancement. A heat exchanger tube with louvered strip inserts was proposed by Fan et al. [29]. The flow resistance, heat transfer, and comprehensive performance of turbulent flow through the tube were numerically investigated. The fluid mixing and boundary disturbance inside the tube were substantially intensified, and the temperature uniformity in the core flow region was thereby significantly improved. Liu et al. [30] proposed the optimal flow field of the longitudinal whirling flow with multi-vortexes. The fluid mixing in the tube would be intensified under the optimal flow field, which led to an improvement in the fluid temperature uniformity. Hence, the fluid temperature gradient near the tube wall was increased and the heat transfer performance inside the tube was enhanced. The above studies demonstrated that intensifying the fluid disturbance is an effective means of enhancing the heat transfer. Therefore, in this study, it is expected that excellent temperature uniformity would be obtained by

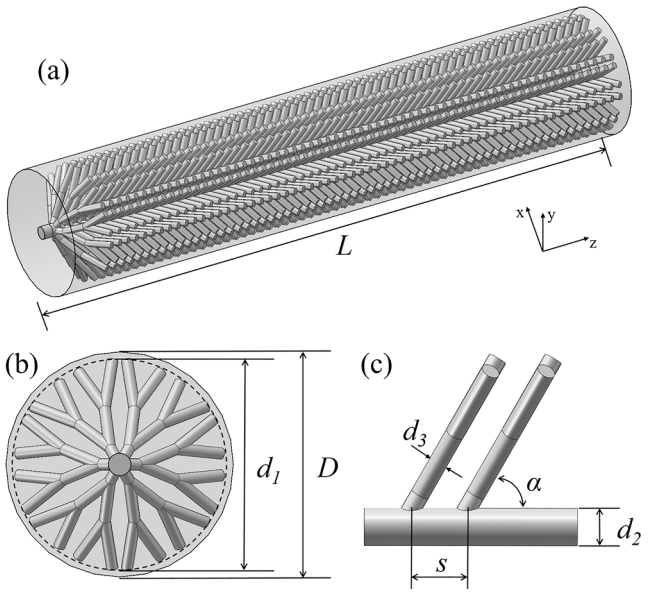


**Fig. 1.** Structure schematic of the T-CBF.

intensifying the fluid disturbance.

To implement the fluid disturbance and the remaining characteristics of the filler, constructal theory was introduced to guide the structure design. Bejan proposed the famous constructal theory in 1997 [31] by analyzing the street network theory of organization [32]. Over the past two decades, the constructal method has been applied extensively in the structure design and optimization of fluid flow channels [33,34], heat conduction elements [35,36], and convection heat transfer elements [37,38]. According to extensive constructal research and practice, the bifurcation shaped structure offers significant potential for heat transfer, and the constructal combination has repeatedly been proven as an effective design method for achieving superior performance.

Inspired by the above-mentioned fluid disturbance intensification method and constructal concept, a constructal bifurcation filler (CBF) based on the secondary combination of a bifurcation shaped structure was proposed for the first time in this study. The CBF was designed to achieve low flow resistance with a high capacity to improve temperature uniformity, with the intention of replacing the porous media filler (PMF) in certain applications. To facilitate the analysis of the heat transfer and flow characteristics of the CBF, as well as evaluate the improvement when using the CBF compared to the PMF, the CBF and PMF were fitted in circular tubes. The flow and heat transfer mechanisms of the two fillers were analyzed. Furthermore, the thermo-hydraulic performances of the two circular tubes with CBF and PMF under the same boundary conditions were numerically investigated and compared. To demonstrate the superiority of the CBF over the porous media further, a comparison was conducted with previous experimental works on heat transfer enhancement by inserting porous media. Finally, the effects of various inclined angles (40°, 50°, 60°, and 70°) and wire mesh pitches (1.5, 2, 2.5, and 3 mm) on the fluid flow and heat transfer characteristics were investigated.

## 2. Geometry model

The structure of the tube with the CBF (T-CBF) is illustrated in Fig. 1. Dozens of layers of wire mesh are attached to the central circular rod at an inclined angle, and each layer of wire mesh includes six independent secondary combination units of bifurcation shaped structure. Longitudinal whirling flow with multi-vortexes is expected to be generated by the secondary combination units of bifurcation shaped structure, therefore, it is anticipated that excellent temperature uniformity will be achieved in the tube. Moreover, the inclined connection between the wire mesh and central circular rod can not only guide the working fluid to generate radial flow and improve the temperature uniformity of the flowing space further, but can also eliminate most of the flow stagnation points and effectively reduce the inertia resistance of the working fluid. In addition, the filler is evenly distributed in space, and its porosity can be adjusted by changing the geometrical parameters. The structure parameters of the T-CBF are listed in Table 1. The diameter of the CBF is 18 mm, which means that the fill radius ratio is 0.9.

**Table 1**
Structure parameters of the T-CBF.

| Structure parameter | Value |
|---|---|
| Tube length $L$ (mm) | 100 |
| Tube diameter $D$ (mm) | 20 |
| Filler diameter $d_1$ (mm) | 18 |
| Central rod diameter $d_2$ (mm) | 2 |
| Wire diameter $d_3$ (mm) | 1 |
| Inclined angle $\alpha$ (°) | 40, 50, 60, 70 |
| Wire mesh pitch $s$ (mm) | 1.5, 2, 2.5, 3 |

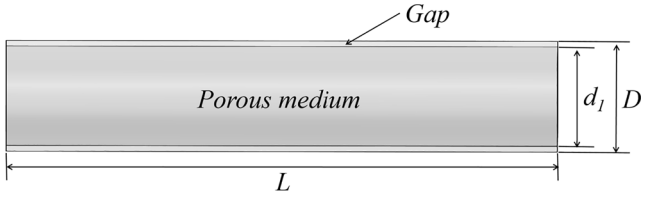


**Fig. 2.** Structure schematic of the T-PMF.

**Table 2**
Structure parameters of the T-PMF.

| Structure parameter | Value |
|---|---|
| Tube length $L$ (mm) | 100 |
| Tube diameter $D$ (mm) | 20 |
| Filler diameter $d_1$ (mm) | 18 |
| Porosity $\varphi$ | 0.69, 0.74, 0.81 |

To evaluate the comprehensive performance improvement of the T-CBF, a tube with the PMF (T-PMF) at the same fill radius ratio and porosity is constructed, as illustrated in Fig. 2. The commonly used woven wire mesh is selected as the porous material. The structure parameters of the T-PMF are summarized in Table 2.

## 3. Numerical method

### 3.1. Governing equations and solution methodology

Helium is selected as the working fluid, which is assumed to be a viscous, compressible, and Newtonian fluid with physical properties that vary with the temperature. Copper is selected as the material of the CBF and PMF due to its high thermal conductivity and large specific heat. Convective heat transfer will occur constantly between the fluid and filler as a result of the internal heat conduction of the filler. Therefore, the following governing equations are used to describe the essence of the flow and heat transfer for the T-CBF.

Continuity equation:

$$\nabla\cdot\left(\rho_f \boldsymbol{U}\right) = 0 \tag{1}$$

Momentum equation:

$$\nabla\boldsymbol{U}\cdot\left(\rho_f \boldsymbol{U}\right) = -\nabla p - \frac{2}{3}\nabla\left[\mu_f(\nabla\cdot\boldsymbol{U})\right] + \nabla\cdot\left[\mu_f(\nabla\boldsymbol{U})^T\right] + \nabla\cdot\left[\mu_f(\nabla\boldsymbol{U})\right] \tag{2}$$

Energy equations:
For the fluid:

$$\rho_f c_p \boldsymbol{U}\cdot\nabla T = \nabla\left[\lambda_f(\nabla T)\right] + \boldsymbol{U}\cdot\nabla p + S \tag{3}$$

For the solid:

$$\nabla[\lambda_s(\nabla T)] - S = 0 \tag{4}$$

In the above, $T$ denotes the temperature; $\lambda_s$ denotes the thermal conductivity of the solid; and $\rho_f$, $\boldsymbol{U}$, $p$, $\mu_f$, $c_p$ and $\lambda_f$ are the density, velocity vector, pressure, dynamic viscosity, specific heat at a constant pressure, and thermal conductivity of the fluid, respectively. Additionally, $S$ represents the convective heat transfer from the solid to fluid, which is expressed as

$$S = h_l(T_s - T_f) \tag{5}$$

where $h_l$ denotes the total heat transfer coefficient between the filler surface and fluid per unit length, and $T_s$ and $T_f$ represent the solid and fluid temperature, respectively.

The RNG $k$-$\varepsilon$ turbulent model is adopted for the computation of the T-CBF because of its excellent prediction capability in a highly swirling pattern and separation prevail flow [39]. The $k$ and $\varepsilon$ equations of the RNG $k$-$\varepsilon$ turbulent model can be expressed as follows according to Ref. [40]:

The $k$ equation:

$$\frac{\partial}{\partial x_i}(\rho_f k u_i) = \frac{\partial}{\partial x_j}\left(\alpha_k \mu_{eff}\frac{\partial k}{\partial x_j}\right) + G_k - \rho_f\varepsilon - Y_M \tag{6}$$

The $\varepsilon$ equation:

$$\frac{\partial}{\partial x_i}(\rho_f \varepsilon u_i) = \frac{\partial}{\partial x_j}\left(\alpha_\varepsilon \mu_{eff}\frac{\partial \varepsilon}{\partial x_j}\right) + C_{1\varepsilon}\frac{\varepsilon}{k}G_k - C_{2\varepsilon}\rho_f\frac{\varepsilon^2}{k} - R_\varepsilon \tag{7}$$

In the above, $Y_M$ represents the contribution of the fluctuating dilatation in compressible turbulence to the overall dissipation rate, and $\alpha_k$ and $\alpha_\varepsilon$ are the inverse effective Prandtl numbers for $k$ and $\varepsilon$, respectively.

The porous model in Fluent 16.0 is employed to simulate the porous zone of the T-PMF. The local thermal equilibrium is adopted by neglecting the temperature difference between the fluid and solid. Therefore, the governing equations for the T-PMF can be expressed as follows:

Continuity equation:

$$\nabla\cdot(\varphi\rho_f\boldsymbol{U}) = 0 \tag{8}$$

Momentum equation:

$$\nabla\boldsymbol{U}\cdot(\varphi\rho_f\boldsymbol{U}) = -\varphi\nabla p - \frac{2}{3}\nabla\left[\varphi\mu_f(\nabla\cdot\boldsymbol{U})\right] + \nabla\cdot\left[\varphi\mu_f\left(\nabla\boldsymbol{U} + (\nabla\boldsymbol{U})^T\right)\right] + \varphi S_f \tag{9}$$

where the final term $S_f$ is composed of the viscous loss part and inertial loss part:

$$S_f = -\left(\frac{\mu_f}{K}\boldsymbol{U} + \frac{C_2}{2}\rho_f|\boldsymbol{U}|\boldsymbol{U}\right) \tag{10}$$

in which $K$ and $C_2$ represent the permeability and inertial resistance coefficient, respectively.

Energy equation:

$$\rho_f c_p \boldsymbol{U}\cdot\nabla T = \nabla\left[\lambda_{eff}(\nabla T)\right] \tag{11}$$

where $\lambda_{eff}$ denotes the effective thermal conductivity.

The permeability $K$ and inertial resistance coefficient $C_2$ are generally calculated from the Darcy-Forchheimer and Darcy equations.

$$\frac{\Delta p}{L} = \frac{\mu_f}{K}u_f + \frac{C_2}{2}\rho_f u_f^2 \tag{12}$$

$$\frac{\Delta p}{L} = \frac{c_f\rho_f u_f^2}{2d_h} \tag{13}$$

where $\Delta p$ and $u_f$ represent the pressure drop and fluid volume average velocity through the porous media, respectively, $d_h$ denotes the hydraulic diameter, and $c_f$ is the friction factor based on the hydraulic diameter.

Tanaka et al. [41] obtained the empirical correlation of the friction factor for a conventional woven wire mesh, which was usually used to calculate the permeability $K$ and inertial resistance coefficient $C_2$.

$$c_f = \frac{175}{Re_h} + 1.60 \tag{14}$$

The Reynolds number $Re_h$ is calculated based on the hydraulic diameter.

$$Re_h = \frac{\rho_f u_f d_h}{\mu_f} \tag{15}$$

By combining Eqs. (12)–(15), the permeability and inertial resistance coefficient can be calculated as follows:

$$K = \frac{2d_h^2}{175} \tag{16}$$

$$C_2 = \frac{1.6}{d_h} \tag{17}$$

The governing equations are discretized using the finite volume method (FVM). The second-order upwind discretization scheme is selected for the continuity, momentum, and energy equations. The pressured-based solver is employed and the SIMPLE algorithm is used to achieve pressure-velocity coupling.

### 3.2. Boundary conditions and parameters definition

To highlight the temperature uniformity of the two types of fillers, the fully developed distributions of the velocity and temperature are employed as the inlet boundary condition. The outlet boundary condition is defined as the pressure outlet to eliminate backflow at the outlet. Moreover, a constant temperature of 500 K and no-slip boundary condition are imposed on the wall, and a thermally coupled wall condition is set at the interface between the solid and fluid.

In this work, the inlet Reynolds number ($Re$) is defined as

$$Re = \frac{u_{in}D\rho_{in}}{\mu_{in}} \tag{18}$$

where $u_{in}$, $\rho_{in}$ and $\mu_{in}$ are the mean velocity, density, and dynamic viscosity of the fluid at the inlet of the tube, respectively.

The logarithmic mean temperature difference between the fluid and wall is calculated as follows:

$$\Delta T_m = \frac{T_{out} - T_{in}}{ln((T_w - T_{in})/(T_w - T_{out}))} \tag{19}$$

where the subscripts *in*, *out*, and *w* indicate the inlet, outlet, and wall, respectively.

The heat transfer coefficient is expressed as

$$h = \frac{q}{\Delta T_m} \tag{20}$$

where $q$ is the heat flux through the wall.

The Nusselt number and friction factor are defined based on the tube diameter using the following formulas:

$$Nu = \frac{hD}{\lambda_f} \tag{21}$$

$$f = \frac{2\Delta pD}{L\rho_f u_f^2} \tag{22}$$

To evaluate the improvement in the comprehensive performance of

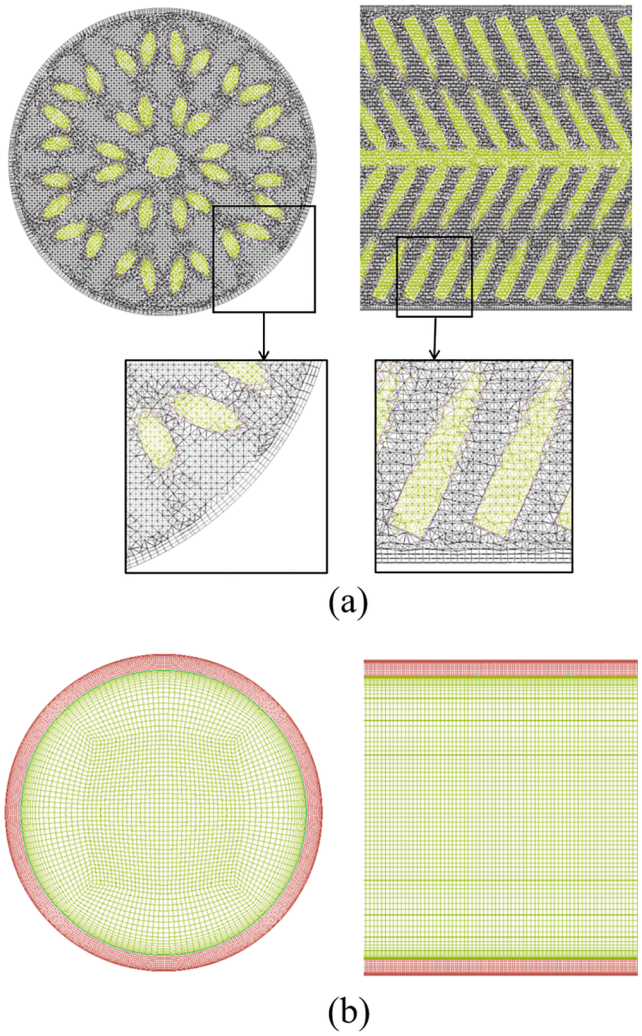


**Fig. 3.** Grid systems: (a) T-CBF and (b) T-PMF.

the T-CBF compared against the T-PMF, the efficiency evaluation criterion [30,42] is defined:

$$EEC = \frac{Nu/Nu_p}{\Delta p/\Delta p_p} \approx \frac{Nu/Nu_p}{f/f_p} \tag{23}$$

where $Nu$ and $Nu_p$ are the Nusselt numbers, and $f$ and $f_p$ are the friction factors for the T-CBF and T-PMF, respectively.

The power consumption caused by the flow resistance is expressed as:

$$P = \Delta p u_f A_i \tag{24}$$

where $A_i$ represents the flow area for the tube inlet.

The dimensionless velocity and dimensionless temperature difference at the middle cross-section of the tube are defined to highlight the uniformity of the velocity and temperature distributions along the radial direction, and are expressed by the following formulas, respectively [17].

$$\overline{u} = \frac{u}{u_m} \tag{25}$$

$$\theta = \frac{T_w - T}{T_w - T_m} \tag{26}$$

where $u$ and $T$ are the local velocity and local temperature at the middle cross-section, respectively, and $u_m$ and $T_m$ are the mean velocity and mean temperature at the middle cross-section, respectively.

**Table 3**
Grid independence tests.

| Grid numbers | $\Delta p$ (Pa) | Deviation of $\Delta p$ | $q$ (W·m$^{-2}$) | Deviation of $q$ |
|---|---|---|---|---|
| *T-CBF* | | | | |
| 8,200,000 | 642.88 | – | 37,477 | – |
| 10,860,000 | 566.49 | −11.88% | 36,158 | −3.52% |
| 13,000,000 | 568.35 | 0.33% | 36,196 | 0.11% |
| 17,950,000 | 575.14 | 1.2% | 36,330 | 0.37% |
| *T-PMF* | | | | |
| 2,830,000 | 3328.7 | – | 7930 | – |
| 4,070,000 | 3528.3 | 6% | 8019 | 1.12% |
| 6,480,000 | 3553.3 | 0.71% | 8067 | 0.6% |

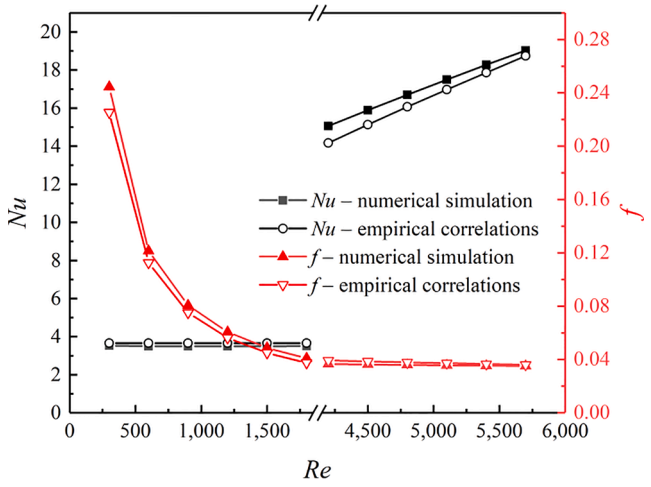


**Fig. 4.** Comparison of the $Nu$ values and $f$ values between the numerical simulation and the empirical correlations for the tube without filler.

### 3.3. Grid generation and independence test

The three-dimensional grid systems for the two types of tubes are generated using the commercial software ICEM, as illustrated in Fig. 3. Tetrahedral grids are applied for the T-CBF considering its complex structure, while hexahedron grids are employed for the T-PMF, as depicted in Fig. 3 (a) and (b), respectively. For the T-CBF, the maximum sizes of the grids in the fluid and solid domains are set to 0.5 and 0.4 mm, respectively. The grids are refined near the wall and interface between the fluid and solid domains, with the maximum grid sizes being 0.05 and 0.3 mm, respectively. For the T-PMF, the maximum grid sizes in the fluid gap and porous region are 0.13 and 0.25 mm, respectively. The grid sizes near the wall and interface between the fluid and porous regions are set to 0.03 mm.

To eliminate the influence of the grid numbers, grid independence tests are conducted for both tube models, the results of which are listed in Table 3. The grid systems with 13 million elements for the T-CBF and 6.48 million elements for the T-PMF are considered to fulfill the computation requirements.

### 3.4. Model validation

Since it is difficult to find published experimental work with similar geometrical and operating parameters to those in this work, the flow and heat transfer characteristics for a tube without a filler are simulated to verify the accuracy of the numerical method. The $Nu$ and $f$ values of the numerical simulation are compared with those obtained from the empirical correlations, which are presented in Eqs. (27) to (30).

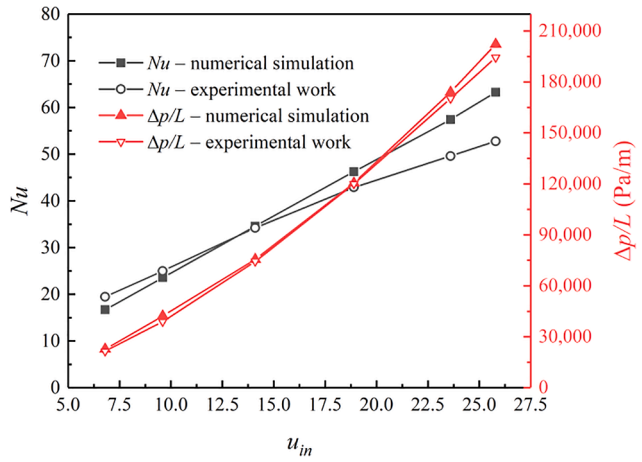


**Fig. 5.** Comparison of $Nu$ and $\Delta p/L$ values between numerical simulation and experimental work for the tube filled with porous media.

**Table 4**
Main geometrical and operating parameters of the tube filled with porous media in experimental work.

| Parameter | $L$ (mm) | $D$ (mm) | $\varphi$ | $K$ ($m^2$) | $C_2$ ($m^{-1}$) | $u_{in}$ ($m{\cdot}s^{-1}$) | $T_{in}$ (K) |
|---|---|---|---|---|---|---|---|
| Value | 400 | 10 | 0.93 | $1 \times 10^{-8}$ | 444 | 7.0–26.0 | 373.2 |

$$Nu = 3.66(\text{laminar}) \tag{27}$$

$$Nu = \frac{(f/8)(Re-1000)Pr}{1+12.7\sqrt{f/8}(Pr^{2/3}-1)}(\text{turbulent}) \tag{28}$$

$$f = \frac{64}{Re}(\text{laminar}) \tag{29}$$

$$\frac{1}{\sqrt{f}} = 2lg(Re\sqrt{f}) - 0.8(\text{turbulent}) \tag{30}$$

Owing to the lack of theoretical or experimental values with sufficient precision under transitional flow, the comparison is conducted under laminar and turbulent flows, as shown in Fig. 4. The numerical simulation results are in good agreement with the empirical correlations, with maximum relative deviations of 6.24% for the $Nu$ value and 8.45% for the $f$ value.

To validate the reliability of the numerical method further, a numerical simulation of the thermo-hydraulic characteristics in a tube filled with porous media using the same numerical method is performed and compared with the results of existing experimental work [43], as shown in Fig. 5. The main geometrical and operating parameters of the tube filled with porous media in the experiment are listed in Table 4. According to Fig. 5, the errors of the $Nu$ and pressure gradient $\Delta p/L$ values between the numerical simulation and experimental work are smaller than 19.9% and 8.6%, respectively. Therefore, in combination with the above validation of the tube without the filler and the tube filled with porous media, it can be concluded that the numerical method presented in this study offers high reliability and accuracy.

## 4. Results and discussion

### 4.1. Analysis of flow and heat transfer mechanisms

Prior to discussing the flow resistance and thermal performance, it is necessary to analyze the flow and heat transfer mechanisms of the two types of tubes, to understand the causes of the differences in the comprehensive performance. Fig. 6 shows the flow characteristics of the T-CBF at $\varphi = 0.74$ and $Re = 600$. As indicated in Fig. 6 (a), a moderate radial velocity component for the fluid is generated by the inclined wire mesh in the entire flow field. This flow pattern will result in a global fluid mass exchange between the boundary flow and core flow region, which intensifies the fluid mixing and leads to an improvement in the fluid temperature uniformity. According to the streamlines at different cross-sections in Fig. 6(b), an obvious local longitudinal whirling flow with multi-vortexes is formed in the entire tube, which is beneficial to the intensification of the local fluid mixing, and hence further improves the temperature uniformity of the flow field.

The effect of the CBF on the thermal performance of the tube is analyzed by means of the fluid temperature distribution of the T-CBF. Fig. 7 displays the temperature distribution characteristics of the T-CBF at $\varphi = 0.74$ and $Re = 600$. Combining the temperature field at the axial section in Fig. 7 (a) and the temperature fields at different cross-sections in Fig. 7 (b), it can be observed that the fluid radial temperature gradient is relatively large near the tube inlet. However, as the distance of the fluid flowing through the CBF increases, the fluid temperature uniformity is rapidly improved due to the longitudinal whirling flow with

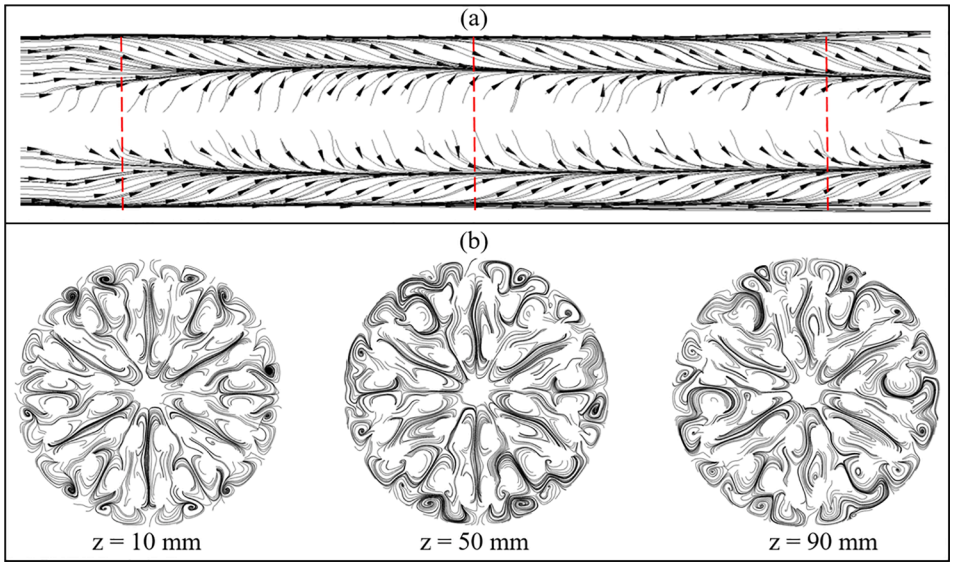


**Fig. 6.** Flow characteristics of the T-CBF at $\varphi = 0.74$ and $Re = 600$: (a) streamline at axial section and (b) streamline at different cross-sections.

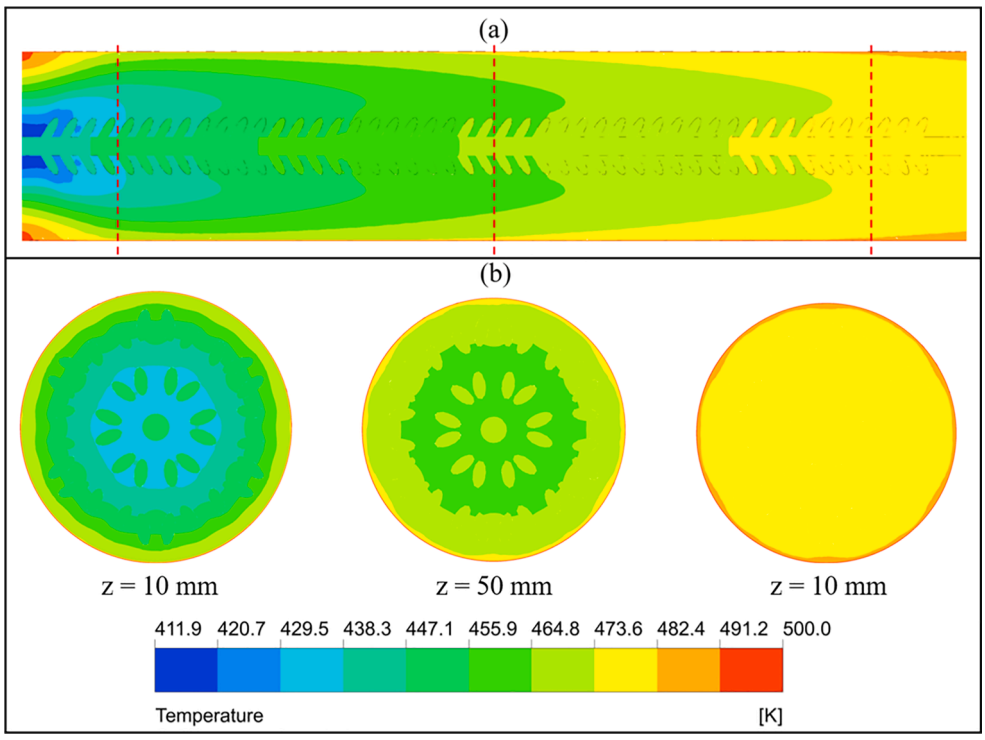


**Fig. 7.** Temperature distribution characteristics of the T-CBF at $\varphi = 0.74$ and $Re = 600$: (a) temperature field at axial section and (b) temperature fields at different cross-sections.

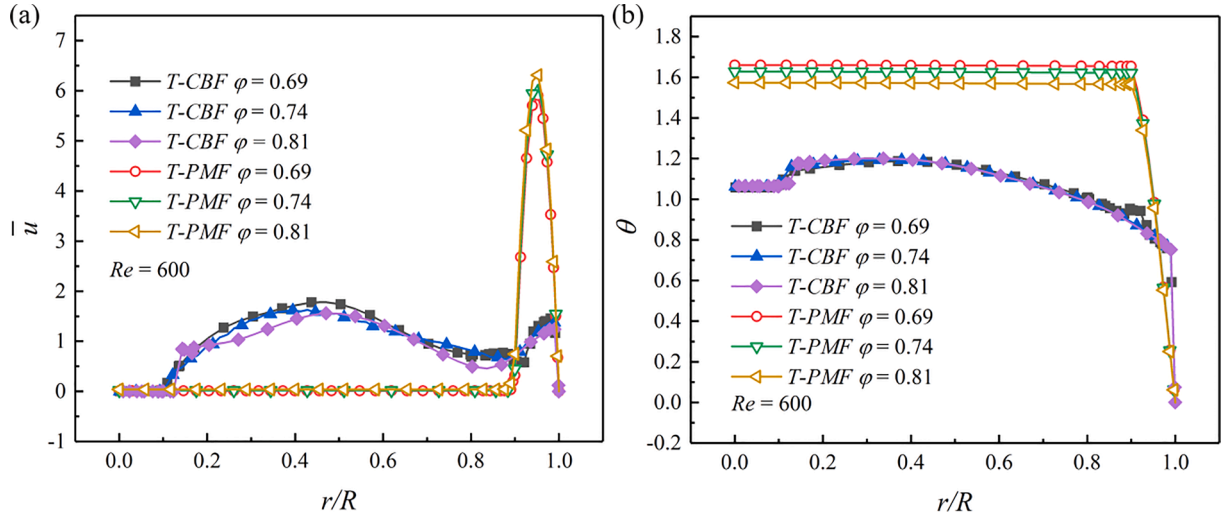


**Fig. 8.** Dimensionless velocity and dimensionless temperature difference profiles at middle cross-sections of the two types of tubes along radial direction.

multi-vortexes, which leads to a decrease in the fluid temperature in the core flow region. Therefore, the fluid temperature gradient near the boundary is significantly increased and the heat transfer is enhanced.

The dimensionless velocity and dimensionless temperature difference profiles at the middle cross-section of the two types of tubes under various porosities (0.69, 0.74, and 0.81) and a constant Reynolds number of $Re = 600$ are calculated to demonstrate the uniformity of the velocity and temperature distributions along the radial direction, as illustrated in Fig. 8. Fig. 8 (a) presents a comparison of the dimensionless velocity distribution at the middle cross-section along the radial direction for the two types of tubes. Most of the fluid flow through the annular channel near the wall in the T-PMF, which means that there is large flow resistance for the fluid flowing through the PMF. However, the velocity distribution at the middle cross-section of the T-CBF is more uniform overall, indicating that the flow resistance for the fluid flowing through the CBF is relatively small. Fig. 8 (b) presents a comparison of the dimensionless temperature difference distribution of the two types of tubes. In both cases, the fluid temperature distribution inside the fillers is highly uniform and the temperature gradient near the boundary increases rapidly, leading to the generation of an equivalent thermal boundary layer and heat transfer enhancement. Therefore, it can be argued that the CBF exhibits excellent temperature uniformity similar to that of the PMF.

The local wall heat flux distributions along the axial direction for the T-CBF and T-PMF at a porosity of $\varphi = 0.74$ and Reynolds number of $Re = 600$ are displayed in Fig. 9. The local heat flux for the T-PMF exhibits a peak value near the inlet and subsequently decreases monotonically along the flow direction. This is because a uniform temperature

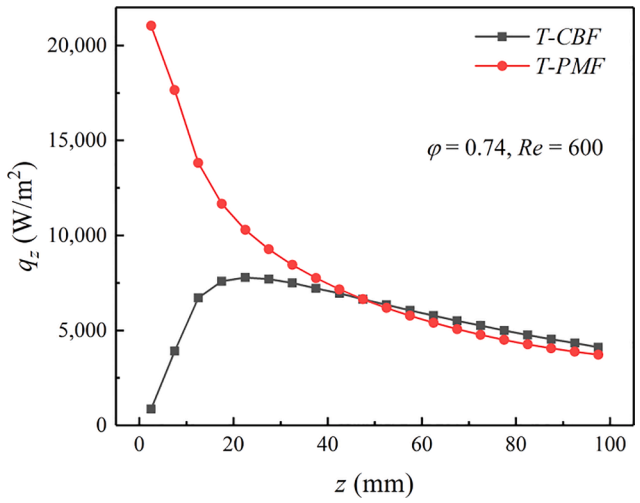


**Fig. 9.** Local wall heat flux distribution along axial direction for the two types of tubes at $\varphi = 0.74$ and $Re = 600$.

distribution for the fluid is developed quickly near the inlet of the T-PMF, causing the maximum temperature gradient in the boundary flow at this point, following which the temperature gradient gradually declines along the flow direction. However, for the T-CBF, the temperature uniformity of the fluid near the inlet is poor, thus, the temperature gradient in the boundary flow is small at this point. When the fluid flows through the filler, the temperature uniformity is rapidly improved, hence, the temperature gradient quickly increases. Thereafter, with the temperature uniformity tending to be steady, the increase in the fluid temperature along the flow direction leads to a decrease in the temperature gradient. As a result, the local wall heat flux for the T-CBF first increases and then decreases along the flow direction. The local heat flux of the T-CBF is less than that of the T-PMF in the front of the tube, whereas there is no significant difference in the local heat flux between the two in the back of the tube. Therefore, in further studies, special attention will be paid to improving the temperature uniformity near the inlet of the T-CBF by ameliorating the CBF structure.

### 4.2. Performance comparison between the T-CBF and T-PMF

After analyzing the flow and heat transfer mechanisms of the two types of tubes, a performance comparison is conducted. The flow resistance characteristics of the T-CBF and T-PMF are illustrated in Fig. 10. Fig. 10 (a) presents a comparison of the pressure drop for the two types of tubes. The pressure drop of the T-CBF decreased significantly compared to that of the T-PMF. The pressure drop ranges are 274–8715 Pa for the T-CBF and 2247–49,497 Pa for the T-PMF within Reynolds numbers of 600–5400. Moreover, the pressure drops of both

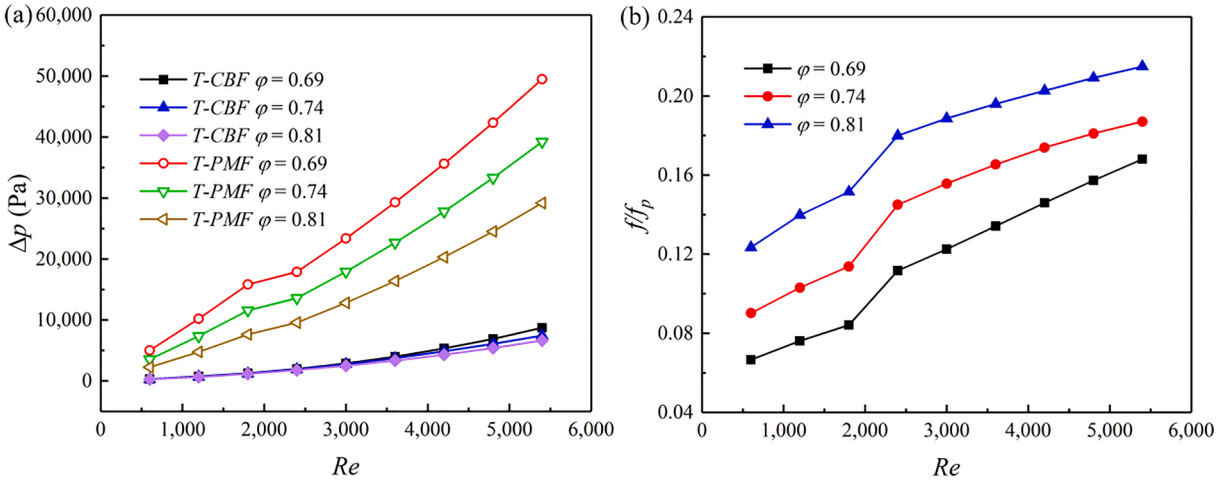


**Fig. 10.** Comparison of flow resistance characteristics of the two types of tubes at different porosities: (a) pressure drop and (b) friction factor ratio.

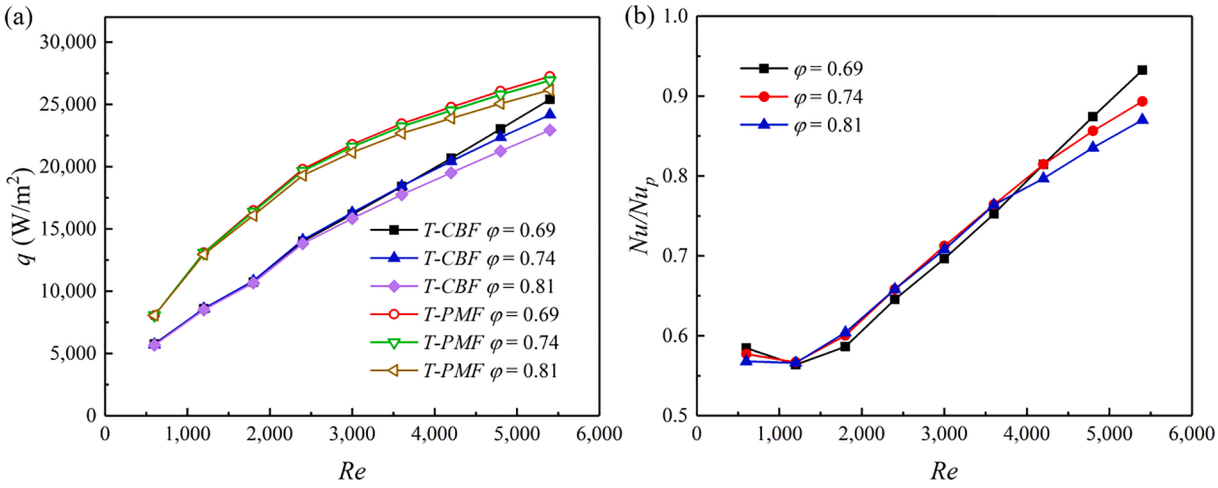


**Fig. 11.** Comparison of heat transfer performance for the two types of tubes at different porosities: (a) wall heat flux and (b) Nusselt number ratio.

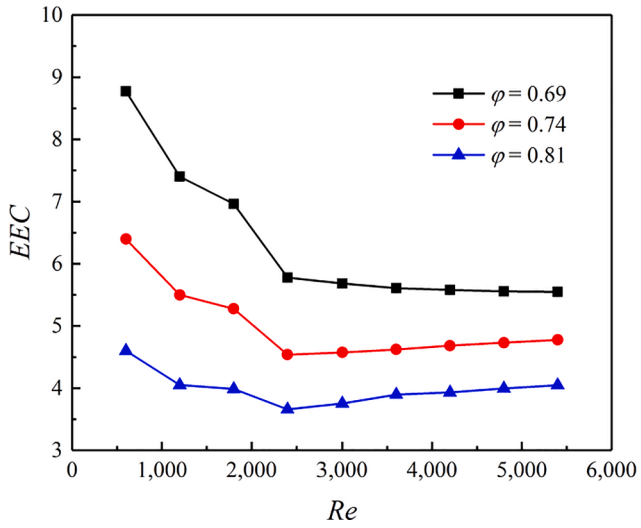


**Fig. 12.** *EEC* values of the T-CBF relative to the T-PMF.

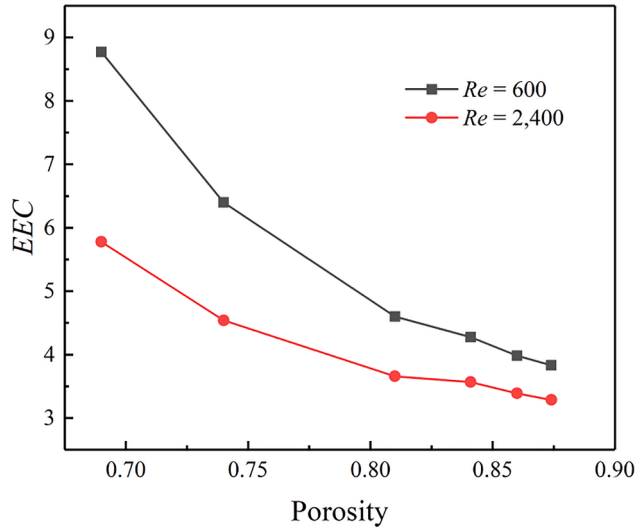


**Fig. 13.** *EEC* values at different porosities.

tubes increase with a decrease in the porosity, and the pressure drop difference between the two types of tubes increases as the porosity decreases. Fig. 10 (b) presents the friction factor ratio ($f/f_p$) of the two types of tubes at different porosities. As shown in Fig. 10 (b), the $f/f_p$ ranges from 0.0667 to 0.2149 within the specified porosity values and Reynolds numbers. Furthermore, $f/f_p$ decreases with decreasing porosity and Reynolds numbers. Thus, it can be concluded that there is lower flow friction for the CBF compared to the PMF, and this advantage is more significant at lower porosity values and Reynolds numbers.

Fig. 11 depicts the wall heat transfer performance of the two types of tubes at different porosities. The wall heat fluxes and Nusselt number ratios of the T-CBF to T-PMF are displayed in Fig. 11 (a) and (b), respectively. Due to the poor temperature uniformity near the inlet, the wall heat flux and Nusselt number of the T-CBF are slightly lower than those of the T-PMF. Furthermore, the effect of the porosity on the heat transfer performance is small, particularly at low Reynolds numbers. This may be because the porosity has little effect on the temperature uniformity at sufficiently low porosity.

The efficiency evaluation criterion (*EEC*), which represents the ratio of the benefit (flow resistance reduction) to the cost (heat transfer performance deterioration) is introduced to compare the comprehensive performance of the two types of tubes. As displayed in Fig. 12, because

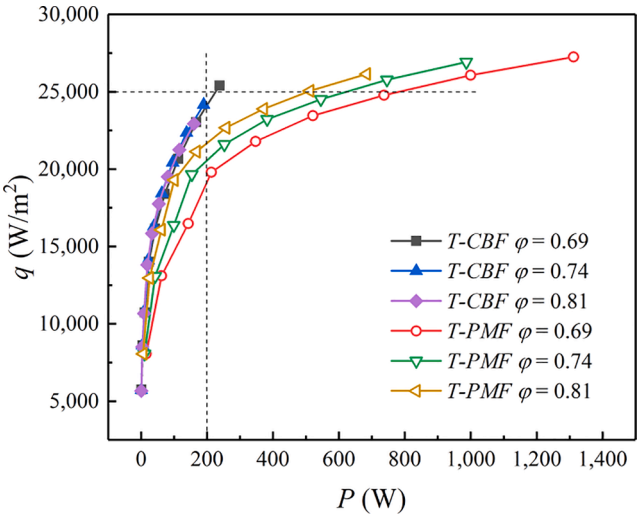


**Fig. 14.** Relationships of wall heat flux and power consumption for the two types of tubes.

the reduction in the flow resistance is significantly greater than that of the heat transfer performance for the T-CBF, the *EEC* value is 3.66–8.77, which is substantially higher than 1, meaning that the comprehensive performance of the T-CBF is substantially improved compared to the T-PMF. Moreover, at a low Reynolds number, the *EEC* value decreases with the increase of the Reynolds number, while at a high Reynolds number, the *EEC* value tends to be constant due to the synchronous increases of the flow resistance and heat transfer ratios for the two types of tubes.

As can be observed from Fig. 12, the *EEC* values are significantly different under various porosities. To understand exactly how the porosity affects the *EEC* value, the *EEC* value versus porosity at $Re = 600$ and 2400 is plotted, as shown in Fig. 13. Under different boundary conditions, the *EEC* value appears to decrease with the increase of the porosity, particularly at a low porosity. This is because the advantage of the low flow resistance of the T-CBF compared to the T-PMF decreases at a high porosity. Therefore, a greater improvement in comprehensive performance for the T-CBF is expected to be obtained at a lower porosity.

The relationships between the wall heat flux and power consumption for the two types of tubes are investigated and displayed in Fig. 14. It can be observed that the wall heat flux of the T-CBF is higher than that of the T-PMF under the same power consumption, that is, lower power consumption is required for the T-CBF compared to the T-PMF when the wall heat fluxes are identical. For instance, the wall heat flux of the T-CBF increases by approximately 26% compared to that of the T-PMF at a power consumption of $P = 200$ W and porosity of $\varphi = 0.69$, or the power consumption of the T-CBF decreases by 71% compared to that of the T-PMF at a wall heat flux of $q = 25{,}000$ W/m$^2$ and porosity $\varphi = 0.69$. Consequently, it is concluded that the sacrifice of the heat transfer rate in the T-CBF is cost-effective due to the considerable reduction in the power consumption.

### 4.3. Comparison with previous experimental works

To demonstrate the superiority of the CBF over porous media further, a comparison with previous experimental works on heat transfer enhancement by filling with porous media, such as wire mesh [44] and metal foam [43], is conducted, as illustrated in Fig. 15. The information regarding the works used in the comparison is listed in Table 5. It can be observed that the thermal performance of the T-CBF is moderate compared to that of the channels filled with porous media in the previous experiments. However, the flow resistance of the T-CBF is much smaller than that of the experimental works, even though the former has

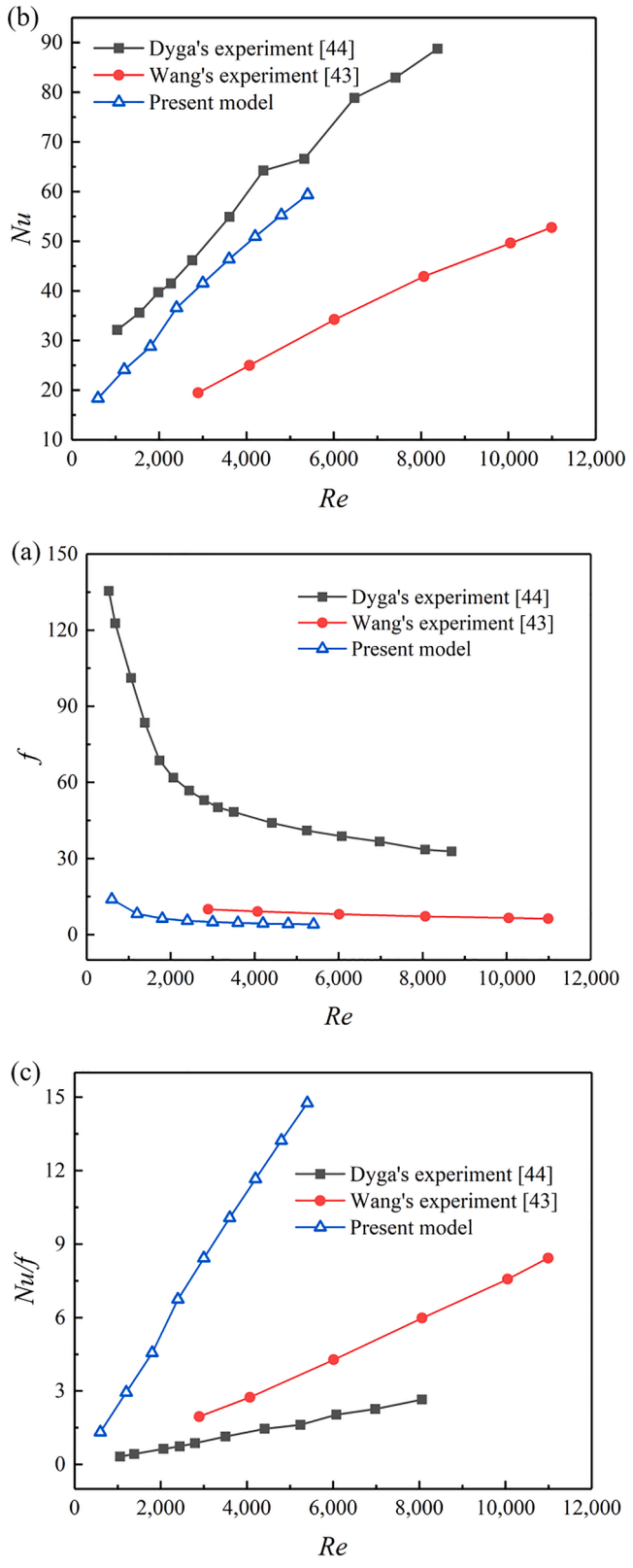


**Fig. 15.** Comparison between present work and previous experimental works: (a) Nusselt number, (b) friction factor, and (c) *Nu/f* value.

a smaller porosity. Hence, the comprehensive thermo-hydraulic performance (*Nu/f*) of the T-CBF is higher than that of the experimental works. In summary, the comparisons between the CBF and porous media in section 4.2 and this section both indicate that the CBF is an effective solution for replacing porous media and diminishing the power consumption.

**Table 5**
Porosity and configuration comparisons between present work and previous experimental works.

| Works | Porosity | Filler configuration |
|---|---|---|
| Dyga's experiment [44] | 0.764 | Wire mesh |
| Wang's experiment [43] | 0.93 | Metal foam |
| Present work | 0.74 | CBF |

### 4.4. *Effects of structure parameters on flow and heat transfer*

The T-CBF with different wire mesh pitches (1.5, 2, 2.5, and 3 mm) is investigated at the same inclined angle of $\alpha = 60°$. Fig. 16 presents the temperature distribution of the axial section of the T-CBF with different wire mesh pitches. As the wire mesh pitch increases, the disturbance of the CBF to the fluid is weakened. Meanwhile, the effective heat conductivity decreases due to the increasing porosity. Consequently, as illustrated in Fig. 16, the average temperature and temperature uniformity of the T-CBF decrease with an increase in the pitch. The gradually improved temperature uniformity increases the temperature difference between the fluid and wall, thereby enhancing the heat transfer performance in the T-CBF, as indicated in Fig. 17 (b). However, as can be observed from Fig. 17 (a), the increasingly intensified disturbance also increases the mechanical energy loss of the fluid, leading to an increase in the pressure drop in the fluid flow. Therefore, it is concluded that the T-CBF with smaller wire mesh pitches exhibits a higher heat transfer rate at the expense of greater flow resistance.

The variation in the wall heat flux with the power consumption is determined to evaluate the comprehensive performance of the T-CBF with different wire mesh pitches, as displayed in Fig. 18. It can be observed that, under the same power consumption, the heat flux of the T-CBF exhibits no significant difference at various pitches. Hence, it can be considered that the thermal performance and power consumption of the T-CBF vary synchronously with the increase of the wire mesh pitch, and the wire mesh pitch has little effect on the comprehensive performance of the T-CBF.

The effects of the inclined angle on the flow resistance and heat transfer characteristics of the T-CBF are investigated at a wire mesh pitch of $s = 3$ mm. Fig. 19 depicts the temperature distribution of the axial section of the T-CBF with different inclined angles. The average temperature and temperature uniformity of the tube first increase and then decrease slightly with an increase in the inclined angle. This may be for two reasons: as the inclined angle increases, on one hand, the fluid mixing intensifies, resulting in an improvement of the temperature uniformity; on the other hand, the heat transfer area between the fluid and wire mesh is diminished, thereby weakening the temperature uniformity to a certain extent. These two opposite effects simultaneously affect the heat transfer performance of the T-CBF.

Fig. 20 shows the pressure drop and wall heat flux of the T-CBF with different inclined angles. As illustrated in Fig. 20 (a), as the inclined angle increases, the pressure drop first increases, and then decreases slightly. The peak value for the pressure drop appears at an inclined angle of $\alpha = 60°$. This should be owing to the inconsistent variations in the viscous resistance and inertial resistance making up the pressure drop. With an increase in the inclined angle, the inertial resistance increases because of the increase in the fluid acceleration, whereas the viscous resistance decreases owing to the reduction in the contact area between the fluid and wire mesh. Therefore, the variation in the pressure drop is dependent on which resistance change is dominant. Before the inclined angle reaches 60°, the inertial resistance change is dominant, leading to an increase of the pressure drop. Thereafter, the viscous resistance change is dominant, resulting in a decrease of the pressure drop. Fig. 20 (b) shows that the wall heat flux of the T-CBF varies

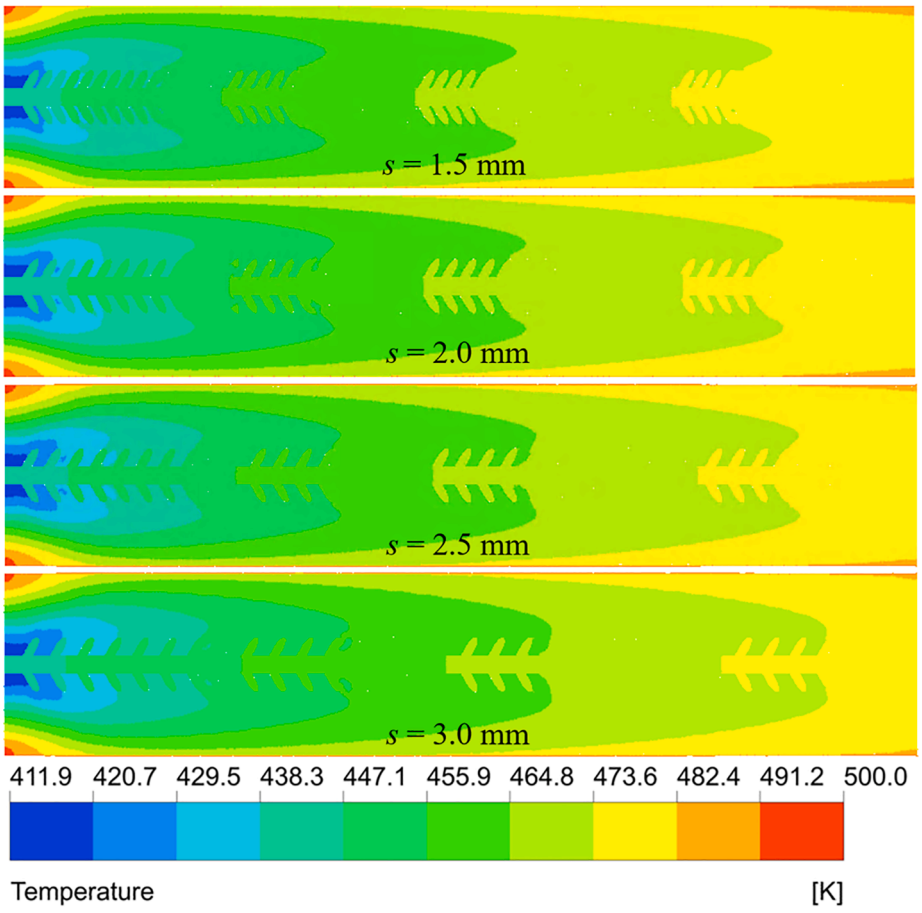


**Fig. 16.** Temperature distribution of axial section of the T-CBF with different wire mesh pitches at $Re = 600$.

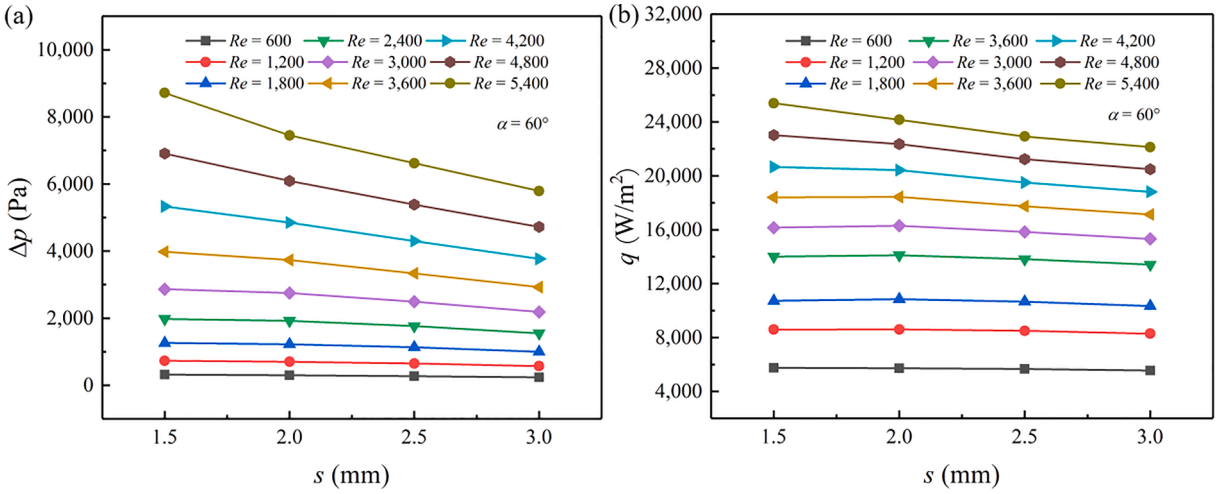


**Fig. 17.** Effects of wire mesh pitch $s$ on pressure drop and wall heat flux for the T-CBF.

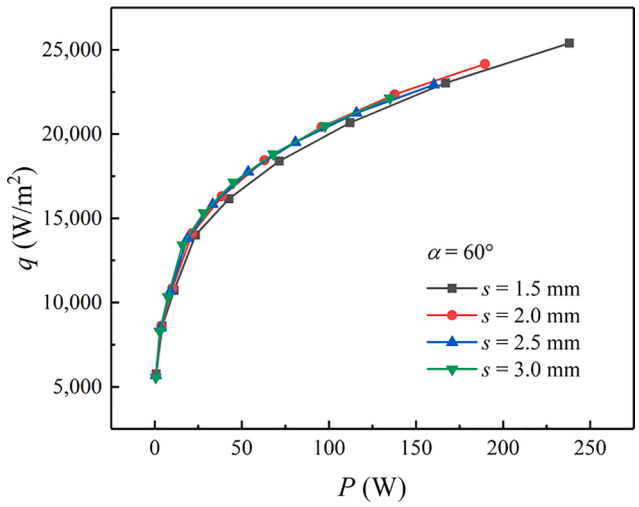


**Fig. 18.** Effect of wire mesh pitch $s$ on comprehensive performance of the T-CBF.

similarly to the pressure drop. This change is dependent on the variation in the temperature uniformity inside the tube, as illustrated in Fig. 19.

The effects of the inclined angle on the comprehensive performance of the T-CBF is reflected by the relationships between the wall heat flux and power consumption, as shown in Fig. 21. The comprehensive performance remains almost unchanged with the inclined angle under low pump power, whereas it increases with an increasing inclined angle under high pump power. Thus, it is reasonable to consider that the inclined angle of $\alpha = 70°$ is the optimal value among the four inclined angles investigated.

## 5. Conclusions

A CBF was proposed as an alternative to the porous media based on constructal concept and fluid disturbance intensification idea. The flow and heat transfer characteristics of the two fillers were numerically investigated and compared. The following conclusions can be drawn:

(1) An obvious longitudinal whirling flow with multi-vortexes is generated by the CBF in the entire tube, which is beneficial for intensifying the fluid mixing and improving the fluid temperature uniformity of the T-CBF. The excellent temperature uniformity leads to a lower fluid temperature in the core flow region and a greater temperature gradient in the boundary flow, resulting in the generation of an equivalent thermal boundary layer and an improvement in the heat transfer performance.

(2) The friction factor ratio of the two types of tubes is 0.0667–0.2149. The flow resistance of the T-CBF is reduced substantially at the cost of a slight reduction in the heat transfer rate. The *EEC* value ranges from 3.66 to 8.77, and the wall heat flux of the T-CBF is higher than that of the T-PMF under the same power consumption. Therefore, the T-CBF exhibits superior comprehensive performance over the T-PMF. The CBF has been proven as a suitable alternative to the PMF for higher energy utilization efficiency.

(3) As the wire mesh pitch increases, both the flow resistance and heat transfer rate of the T-CBF decrease. However, the wire mesh pitch has little effect on the comprehensive performance. As the

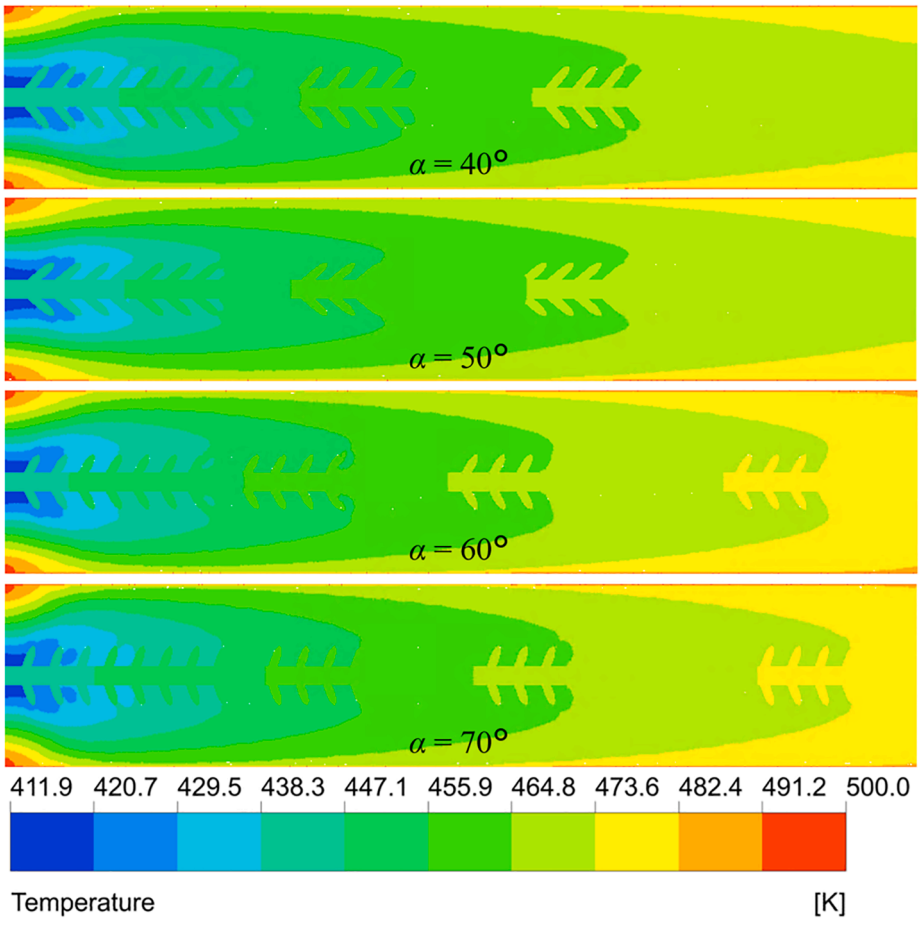


**Fig. 19.** Temperature distribution of axial section of the T-CBF with different inclined angles at $Re = 600$.

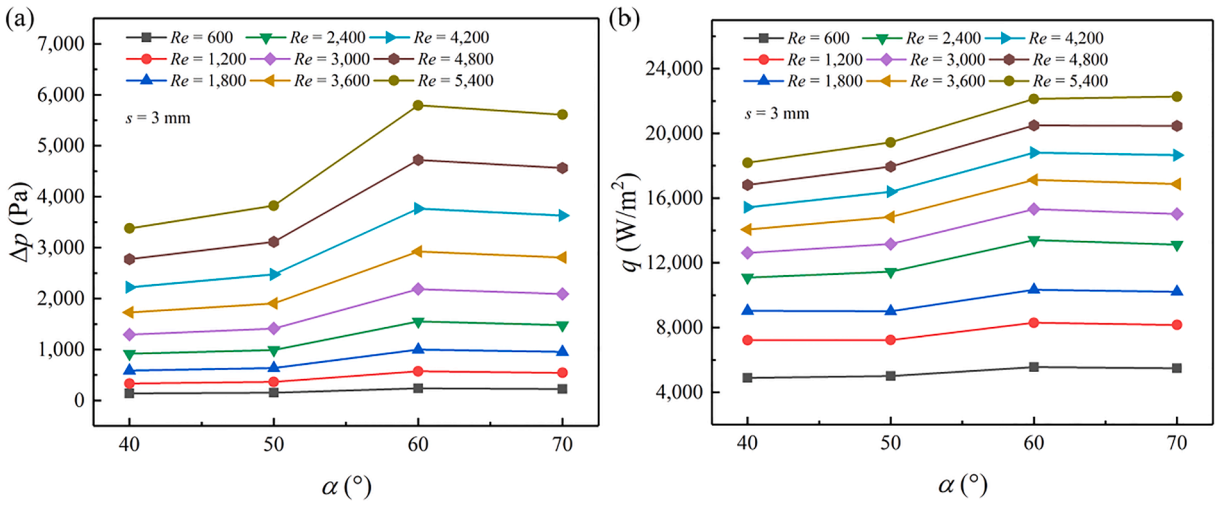


**Fig. 20.** Effects of inclined angle $\alpha$ on pressure drop and wall heat flux for the T-CBF.

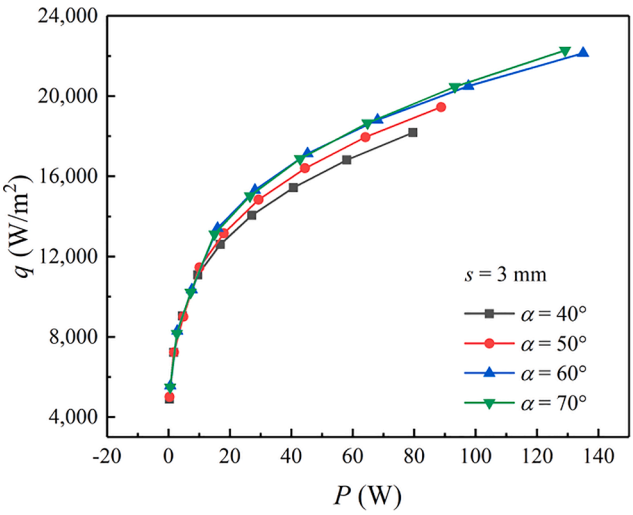


**Fig. 21.** Effect of inclined angle $\alpha$ on comprehensive performance of the T-CBF.

inclined angle increases, the flow resistance and heat transfer rate first increase and then decrease slightly. Both peak values appear when the inclined angle is 60°. The comprehensive performance increases with an increase in the inclined angle.

## Declaration of Competing Interest

The authors declare that they have no known competing financial interests or personal relationships that could have appeared to influence the work reported in this paper.

## Acknowledgment

This work was supported by the key project of National Natural Science Foundation of China (Grant No. 51736004).

## References

[1] S. Rashidi, M.H. Kashefi, K.C. Kim, O. Samimi-Abianeh, Potentials of porous materials for energy management in heat exchangers – a comprehensive review, Appl. Energy 243 (2019) 206–232.
[2] H. Yang, J. Wen, S. Wang, Y. Li, Effect of fin types and Prandtl number on performance of plate-fin heat exchanger: Experimental and numerical assessment, Appl. Therm. Eng. 144 (2018) 726–735.
[3] K. Guo, N. Zhang, R. Smith, Design optimisation of multi-stream plate fin heat exchangers with multiple fin types, Appl. Therm. Eng. 131 (2018) 30–40.
[4] M.M. Sarafraz, M. Arjomandi, Contact angle and heat transfer characteristics of a gravity-driven film flow of a particulate liquid metal on smooth and rough surfaces, Appl. Therm. Eng. 149 (2019) 602–612.
[5] K. Nanan, C. Thianpong, M. Pimsarn, V. Chuwattanakul, S. Eiamsa-ard, Flow and thermal mechanisms in a heat exchanger tube inserted with twisted cross-baffle turbulators, Appl. Therm. Eng. 114 (2017) 130–147.
[6] P. Liu, N. Zheng, F. Shan, Z. Liu, W. Liu, An experimental and numerical study on the laminar heat transfer and flow characteristics of a circular tube fitted with multiple conical strips inserts, Int. J. Heat Mass Transf. 117 (2018) 691–709.
[7] Y. Liang, P. Liu, N. Zheng, F. Shan, Z. Liu, W. Liu, Numerical investigation of heat transfer and flow characteristics of laminar flow in a tube with center-tapered wavy-tape insert, Appl. Therm. Eng. 148 (2019) 557–567.
[8] M. Sheikholeslami, E. Abohamzeh, M. Jafaryar, A. Shafee, H. Babazadeh, CuO nanomaterial two-phase simulation within a tube with enhanced turbulator, Powder Technol. 373 (2020) 1–13.
[9] M. Sheikholeslami, S.A. Farshad, A. Shafee, H. Babazadeh, Numerical modeling for nanomaterial behavior in a solar unit analyzing entropy generation, J. Taiwan Inst. Chem. Eng. 112 (2020) 271–285.
[10] J. Tang, X. Hu, Evaluation of capillary wetting performance of micro-nano hybrid structures for open microgrooves heat sink, Exp. Therm Fluid Sci. 112 (2020), 109948.
[11] S. Zarei, H.R. Talesh Bahrami, H. Saffari, Effects of geometry and dimension of micro/nano-structures on the heat transfer in dropwise condensation: A theoretical study, Appl. Therm. Eng. 137 (2018) 440–450.
[12] P. Vivekh, M. Kumja, D.T. Bui, K.J. Chua, Recent developments in solid desiccant coated heat exchangers – a review, Appl. Energy 229 (2018) 778–803.
[13] M. Torabi, N. Karimi, G.P. Peterson, S. Yee, Challenges and progress on the modelling of entropy generation in porous media: a review, Int. J. Heat Mass Transf. 114 (2017) 31–46.
[14] H.J. Xu, Z.B. Xing, F.Q. Wang, Z.M. Cheng, Review on heat conduction, heat convection, thermal radiation and phase change heat transfer of nanofluids in porous media: fundamentals and applications, Chem. Eng. Sci. 195 (2019) 462–483.
[15] M. Dehghan, M.S. Valipour, S. Saedodin, Microchannels enhanced by porous materials: heat transfer enhancement or pressure drop increment? Energy Convers. Manage. 110 (2016) 22–32.
[16] M.H. Mohammadi, H.R. Abbasi, A. Yavarinasab, H. Pourrahmani, Thermal optimization of shell and tube heat exchanger using porous baffles, Appl. Therm. Eng. 170 (2020), 115005.
[17] Z.F. Huang, A. Nakayama, K. Yang, C. Yang, W. Liu, Enhancing heat transfer in the core flow by using porous medium insert in a tube, Int. J. Heat Mass Transf. 53 (5-6) (2010) 1164–1174.
[18] M. Sheikholeslami, M. Jafaryar, A. Shafee, H. Babazadeh, Acceleration of discharge process of clean energy storage unit with insertion of porous foam considering nanoparticle enhanced paraffin, J. Cleaner Prod. 261 (2020), 121206.
[19] Z.-B. Liu, Y.-L. He, Z.-G. Qu, W.-Q. Tao, Experimental study of heat transfer and pressure drop of supercritical CO2 cooled in metal foam tubes, Int. J. Heat Mass Transf. 85 (2015) 679–693.
[20] W. Tu, Y. Wang, Y. Tang, J. Xu, Heat transfer and pressure drop characteristics in a circular tube with mesh cylinder inserts, Int. Commun. Heat Mass Transfer 75 (2016) 130–136.
[21] S. Baragh, H. Shokouhmand, S.S.M. Ajarostaghi, M. Nikian, An experimental investigation on forced convection heat transfer of single-phase flow in a channel with different arrangements of porous media, Int. J. Therm. Sci. 134 (2018) 370–379.

[22] S. Baragh, H. Shokouhmand, S.S.M. Ajarostaghi, Experiments on mist flow and heat transfer in a tube fitted with porous media, Int. J. Therm. Sci. 137 (2019) 388–398.
[23] Z. Cao, J. Xu, Modulated heat transfer tube with short conical-mesh inserts: a linking from microflow to macroflow, Int. J. Heat Mass Transf. 89 (2015) 291–307.
[24] J. He, Z. Chen, X. Jiang, C. Leng, Combustion characteristics of blast furnace gas in porous media burner, Appl. Therm. Eng. 160 (2019), 113970.
[25] Q. Ma, Q. Xu, Q. Chen, Z. Chen, H. Su, W. Zhang, Lattice Boltzmann model for complex transfer behaviors in porous electrode of all copper redox flow battery with deep eutectic solvent electrolyte, Appl. Therm. Eng. 160 (2019), 114015.
[26] G. Xiao, H. Peng, H. Fan, U. Sultan, M. Ni, Characteristics of steady and oscillating flows through regenerator, Int. J. Heat Mass Transf. 108 (2017) 309–321.
[27] P.W. Deshmukh, S.V. Prabhu, R.P. Vedula, Heat transfer enhancement for laminar flow in tubes using curved delta wing vortex generator inserts, Appl. Therm. Eng. 106 (2016) 1415–1426.
[28] P.W. Deshmukh, R.P. Vedula, Heat transfer and friction factor characteristics of turbulent flow through a circular tube fitted with vortex generator inserts, Int. J. Heat Mass Transf. 79 (2014) 551–560.
[29] A.W. Fan, J.J. Deng, A. Nakayama, W. Liu, Parametric study on turbulent heat transfer and flow characteristics in a circular tube fitted with louvered strip inserts, Int. J. Heat Mass Transf. 55 (19-20) (2012) 5205–5213.
[30] W. Liu, P. Liu, J.B. Wang, N.B. Zheng, Z.C. Liu, Exergy destruction minimization: a principle to convective heat transfer enhancement, Int. J. Heat Mass Transf. 122 (2018) 11–21.
[31] A. Bejan, Constructal-theory network of conducting paths for cooling a heat generating volume, Int. J. Heat Mass Transf. 40 (4) (1997) 799–816.
[32] A. Bejan, Street network theory of organization in nature, ATR 30 (2) (1996) 85–107.
[33] A. Bejan, L. Rocha, S. Lorente, Thermodynamic optimization of geometry: T-and Y-shaped constructs of fluid streams, Int. J. Therm. Sci. 39 (2000) 949–960.
[34] L. Chen, H. Feng, Z. Xie, F. Sun, Thermal efficiency maximization for H- and X-shaped heat exchangers based on constructal theory, Appl. Therm. Eng. 91 (2015) 456–462.
[35] S. Zhou, L. Chen, F. Sun, Optimization of constructal volume-point conduction with variable cross section conducting path, Energy Convers. Manage. 48 (1) (2007) 106–111.
[36] L. Chen, H. Feng, Z. Xie, F. Sun, Progress of constructal theory in China over the past decade, Int. J. Heat Mass Transf. 130 (2019) 393–419.
[37] X. Zhang, D. Liu, Optimum geometric arrangement of vertical rectangular fin arrays in natural convection, Energy Convers. Manage. 51 (12) (2010) 2449–2456.
[38] H. Feng, L. Chen, Z. Xie, F. Sun, Constructal design for helm-shaped fin with internal heat sources, Int. J. Heat Mass Transf. 110 (2017) 1–6.
[39] M. Tutar, A.E. Holdø, Computational modelling of flow around a circular cylinder in sub-critical flow regime with various turbulence models, Int. J. Numer. Meth. Fluids 35 (7) (2001) 763–784.
[40] V. Yakhot, S.A. Orszag, Renormalization group analysis of turbulence: I. Basic theory, J. Sci. Comput. 1 (1) (1986) 3–51.
[41] M. Tanaka, I. Yamashita, F. Chisaka, Flow and heat transfer characteristics of the stirling engine regenerator in an oscillating Flow, JSME Int. J. 33 (1990) 283–289.
[42] W. Liu, P. Liu, Z.M. Dong, K. Yang, Z.C. Liu, A study on the multi-field synergy principle of convective heat and mass transfer enhancement, Int. J. Heat Mass Transf. 134 (2019) 722–734.
[43] H. Wang, L. Guo, Experimental investigation on pressure drop and heat transfer in metal foam filled tubes under convective boundary condition, Chem. Eng. Sci. 155 (2016) 438–448.
[44] R. Dyga, M. Płaczek, Efficiency of heat transfer in heat exchangers with wire mesh packing, Int. J. Heat Mass Transf. 53 (23-24) (2010) 5499–5508.